TRUST-DART: Land Surfaces Temperature and Emissivity Nonlinear Mapping from Non-isothermal Mixed Pixels of Satellite Images with the DART 3D Radiative Transfer Model

Zhijun Zhen [1,2], Jonathan León-Tavares [3], Abdelaziz Kallel [4], Yingjie Wang [1], Omar Regaieg [1,5], Eric Chavanon [1], Nicolas Lauret [1], Jordan Guilleux [1], Johan Hedman [1], Tiangang Yin [6], Romain Demoulin [1], Jean-Philippe Gastellu-Etchegorry [1]

[1] CESBIO, Université de Toulouse, UT3-Paul Sabatier/CNES/CNRS/INRAE/IRD, 18, Avenue Edouard Belin, 31401 Toulouse, France – (zhijun.zhen, yingjie.wang, eric.chavanon, nicolas.lauret, jordan.guilleux, romain.demoulin)@univ-tlse3.fr; johan.hedman@ensta-paris.fr; jean-philippe.gastellu@iut-tlse3.fr
[2] College of Geoexploration Science and Technology, Jilin University, Changchun, 130026, China – zhenzj18@mails.jlu.edu.cn
[3] Vlaamse Instelling voor Technologisch Onderzoek (VITO), Boeretang 200, 2400 Mol, Belgium – jonathan.leontavares@vito.be
[4] Laboratory of Signals, Systems Artificial Intelligence and Networks (SM@RTS), Digital Research Centre of Sfax, Sfax 3021, Tunisia – abdelaziz.kallel@crns.rnrt.tn
[5] Remote Sensing Research Group, Department of Geography, University of Bonn, Meckenheimer Allee 166, Bonn 53115, Germany – oregaieg@uni-bonn.de
[6] Department of Land Surveying and Geo-Informatics, The Hong Kong Polytechnic University, Hung Hom, Hong Kong – tiangang.yin@polyu.edu.hk

Keywords: Urban, Temperature, Emissivity, DART, Satellite image, Thermal unmixing.

Abstract

Coarse spatial resolution of Thermal Infrared (TIR) satellites hampers measuring the temperature and emissivity of scene elements from space that improves our understanding of land surfaces' thermal behavior. The stringent conditions of current TIR unmixing methods hinder the production of extensive component temperature and emissivity products. To address this, we designed a gradient-based multi-pixel physical model, TRUST-DART, to derive the temperature and emissivity of urban features from non-isothermal mixed pixels of satellite images using the DART 3D radiative transfer model. Unlike traditional TIR unmixing methods, TRUST-DART is not constrained by issues related to spatial, spectral, temporal resolution, angular, scene, field measurement requirements, or manual operations. Its inputs include an at-surface radiance image, downwelling sky irradiance, a 3D urban mock-up with feature information, and DART input parameters such as spatial resolution. It generates maps of emissivity and temperature per urban feature. Its accuracy is validated for two vegetation and urban scenes and two types of images (DART simulated pseudo satellite and ASTER observed images). The accuracy of the TRUST-DART depends heavily on the fraction of components. TRUST-DART proves robust for high-fraction components. However, its accuracy decreases with decreasing fractions. TRUST-DART is distributed with DART and is available for education and research via Toulouse III University (https://dart.omp.eu).

1. Introduction

In thermal remote sensing, the emissivity and temperature of scene elements are crucial quantities for understanding plant physiological processes and the thermal behavior of urban environments (Jiang et al., 2022; Song et al., 2020). They are vital inputs for evapotranspiration models (Chen and Liu, 2020; Sánchez et al., 2008) and can help monitor variations in urban materials and structures (Huang et al., 2017; Ru et al., 2023).

The separation of Land Surface Emissivity (LSE) and Land Surface Temperature (LST) from pixels is a complex problem, addressed by many methods categorized as either "stepwise" or "simultaneous". Stepwise methods, such as single-channel (Ottlé and Vidal-Madjar, 1992), multi-channel (McMillin, 1975), and multi-angle methods (Sobrino and Romaguera, 2004), first determine LSE, then retrieve LST using the determined LSE. However, these methods may introduce significant errors in the retrieved LST when the error in LSE is substantial. On the other hand, simultaneous methods, including the temperature and emissivity separation method (Gillespie et al., 1998), the two-temperature method (TTM) (Watson, 1992), and the physics-based day/night operational method (Wan and Li, 1997), can retrieve both temperature and emissivity simultaneously. This approach generally results in higher temperature and emissivity retrieval accuracy than stepwise methods. However, these methods operate under the assumption of pure, isothermal, and flat pixels, an assumption that is challenging to fulfill in TIR images over urban areas due to the coarse spatial resolutions (Zhen et al., 2022) and high heterogeneity of urban environments (Ru et al., 2023). Compared to homogeneous validation sites, the separated temperature and emissivity data accuracy significantly decreases when the validation sites are heterogeneous (Hu et al., 2022).

Extracting component temperature and emissivity data from current satellite imagery is a valuable yet complex task. Challenges arise due to factors such as ambiguous definitions of pixel and component emissivity (Norman and Becker, 1995), the temperature within mixed pixels (Li et al., 1999), emissivity directionality (Cao et al., 2019), and the uncertainties introduced by the unmixing process (Fontanilles and Briottet, 2011). For a TIR multispectral image with Λ bands measured over a mixed pixel containing I components, the unknowns include I component temperatures, $I-1$ fraction values (*i.e.*, area fraction) per component, and $\Lambda \times I$ component emissivity values. These unknowns greatly outnumber the Λ equations.

Several methods have been proposed to unmix component emissivity and temperature, including multi-angular, multispectral, multi-temporal, multi-pixel, and multi-resolution temperature unmixing methods (Zhan et al., 2013). Each method has its limitations and requirements: multi-angle unmixing method requires multi-angle data (Jacob et al., 2008; Kimes, 1983), often lacking time continuity. It is designed for specific vegetation types and geometrical structures, making it

challenging to parameterize analytically. Multispectral unmixing methods (Gillespie, 1992) are for specific land surface types with known component emissivity values. Multi-temporal methods (Zhan et al., 2012) require the LST diurnal cycle to be parameterized. Sometimes, real-time ground records are needed to assist multi-temporal unmixing in case of inadequate time observations. Multi-pixel (Dozier, 1981) and multi-resolution (Archer and Jones, 2006) unmixing methods assume that component temperatures do not change within a specific spatial scale. Multi-pixel unmixing methods leverage the geographical correlation among component temperatures of adjacent pixels, where the associated component fractions vary from pixel to pixel. The multi-resolution unmixing method utilizes multi-resolution data. However, most studies only consider soil and vegetation, limiting applications over heterogeneous terrain.

A variety of sophisticated techniques have been introduced to unmix component temperature and emissivity across diverse land surfaces. For instance, the Thermal Remote Sensing Unmixing for Subpixel Temperature (TRUST) method (Cubero-Castan et al., 2014) and its multitemporal variant, TRUST Day and Night Synergy (TRUST-DNS) (Granero-Belinchon et al., 2020), perform estimations in straightforward scenarios. Current TIR satellite resolutions limit the use of TRUST and TRUST-DNS for generating component temperature products. The TRISHNA mission offers a 60 m resolution with 4 bands, below the 1 m with 30 bands needed by TRUST and 8 m with 8 bands by TRUST-DNS. Both models assume spatial invariant emissivity and linear unmixing, making them unsuitable for complex urban environments with multiple scattering.

In view of the limitations of existing TIR unmixing methods, this study introduces a comprehensive multi-pixel TIR nonlinear unmixing model named TRUST-DART. It is a gradient-based multi-pixel physical model that simultaneously separates component temperature and emissivity over both vegetation and urban areas. It is a TIR adaptation of a DART inversion algorithm (Landier et al., 2018; Zhen et al., 2021) used for energy exchange monitoring in the shortwave domain (Chrysoulakis et al., 2018). In addition to DART common input data (*e.g.*, downwelling sky irradiance (E_λ) and spatial resolution), it has two major input data: an at-surface radiance image (L_λ), and a 3D mock-up with component classification information. TRUST-DART provides maps of component emissivity and temperature. Incorporating knowledge from computer graphics, deep learning, and geostatistics, it greatly contributes to the field:

- A novel solution to overcome constraints of TIR unmixing methods on sensor configuration such as spatial, temporal, and spectral resolutions, as well as multi-angular observations.
- The gradient-based nonlinear unmixing model separates component temperature and emissivity by considering the multiple scattering using propagating gradients among parameters with distinct physical interpretations.
- Easier simultaneous separation of component emissivity and temperature, considering spatial variability.

TRUST-DART is first presented after a brief presentation of DART. Its validity is tested with a vegetation scene and an urban scene, using pseudo-satellite images simulated by the DART model and an Advanced Spaceborne Thermal Emission and Reflection Radiometer (ASTER) satellite image.

2. Methodology and Data

2.1 DART Model

DART is a comprehensive and precise 3D radiative transfer model grounded in physics. It facilitates the simulation of Earth-atmosphere radiation interactions, spanning from visible to TIR wavelengths, across both urban and natural landscapes, considering atmospheric and topographic conditions (Gastellu-Etchegorry et al., 2022; Gastellu-Etchegorry et al., 2020a, b; Wang et al., 2024; Zhen et al., 2023). Initiated at CESBIO in 1992 and patented in 2003, DART is readily accessible for non-commercial academic and research purposes via the University of Toulouse's website (https://dart.omp.eu).

2.2 Methodology

TRUST-DART uses an iterative optimization algorithm to unmix component temperature and emissivity from mixed pixels in thermal remote-sensing multispectral images. It has three key modules: pure pixel selection (PPS), Jacobian iterations (JI), and spectral correlation (SC) module (Figure 1). The PPS module provides the initial emissivity ($\varepsilon_{i,\lambda}^{\mathrm{PPS}}$) and temperature ($T_i^{\mathrm{PPS}}$) of each component in the scene, derived from pure pixels. Then, the Jacobian iteration module refines these initial values to $\varepsilon_{i,\lambda}^{\mathrm{JI}}$ and T_i^{JI}. Input parameters of TRUST-DART include a 3D urban mock-up with component class labels, an at-surface radiance image $L_{\mathrm{sat},\lambda}$ and scene irradiance E_λ. Finally, TRUST-DART gives component temperature T_i and emissivity $\varepsilon_{i,\lambda}$ maps. TRUST-DART modules are presented below.

2.2.1 Pure Pixel Selection (PPS) Module: It derives $\varepsilon_{i,\lambda}^{\mathrm{PPS}}$ and T_i^{PPS} per urban component *i*, using pure pixels in LSE and LST images, either directly provided or derived from satellite radiance image $L_{\mathrm{sat},\lambda}$ and irradiance E_λ using the TES method. The process begins with a DART simulation to determine the purity percentage S_i of component *i* per pixel. Then, pure pixels for each *i* are chosen based on their value S_i. The initial threshold of S_i is set at 0.9. If this threshold fails to select any pure pixels, it is gradually reduced from 0.9 to 0.1 in steps of 0.1. If no pure pixel is identified even at the minimum threshold, the emissivity and temperature specified by the users in the DART simulation for calculating S_i are given to $\varepsilon_{i,\lambda}^{\mathrm{PPS}}$ and T_i^{PPS}. The values of $\varepsilon_{i,\lambda}^{\mathrm{PPS}}$ and T_i^{PPS} from the mixed pixels are determined by the value of the nearest (in terms of Euclidean distance) pure pixel. If multiple pure pixels are selected as the nearest pure pixel, the median value of all nearest pure pixels is used. The underlying rationale for these operations is the principle of spatial continuity for each component. Due to co-registration discrepancies between DART and satellite imagery, some pixels at the periphery of DART images may be detected as pure without being so. Consequently, an erosion process can be employed for images with very high spatial resolution that possess an adequate number of pure pixels, thereby ensuring the purification of the selected pixels.

2.2.2 Jacobian Iteration (JI) Module: It uses Jacobians (*i.e.*, partial derivatives), DART simulated radiance $L_{\mathrm{DART},\lambda}^{j+1}$ at the next iteration j+1 is

$$L_{\mathrm{DART},\lambda}^{j+1}=L_{\mathrm{DART},\lambda}^{j}+\sum_{i=1}^{I} G_{\varepsilon,i,\lambda}^{j}\cdot\left(\varepsilon_{i,\lambda}^{j+1}-\varepsilon_{i,\lambda}^{j}\right)+\sum_{i=1}^{I} G_{T,i,\lambda}^{j}\cdot\left(T_i^{j+1}-T_i^{j}\right), \quad (1)$$

where i = element index
j = iteration index
λ = band index
ε = emissivity
T = thermodynamic temperature

$L^j_{\mathrm{DART},\lambda}$ = DART simulated radiance image
$G^j_{\varepsilon,i,\lambda}$ = gradient calculated with $\varepsilon^j_{i,\lambda}$
$G^j_{T,i,\lambda}$ = gradient calculated with T_i^j

At iteration j, the inversion must provide $\varepsilon^{j+1}_{i,\lambda}$ and T_i^{j+1} such that DART $L^{j+1}_{\mathrm{DART},\lambda}$ and satellite $L_{\mathrm{sat},\lambda}$ radiance images are equal:

$$L_{\mathrm{sat},\lambda}=L^j_{\mathrm{DART},\lambda}+\sum_{i=1}^{I} G^j_{\varepsilon,i,\lambda}\cdot\left(\varepsilon^{j+1}_{i,\lambda}-\varepsilon^j_{i,\lambda}\right)+\sum_{i=1}^{I} G^j_{T,i,\lambda}\cdot\left(T_i^{j+1}-T_i^j\right), \quad (2)$$

In Eq.(2), the only unknowns are $\varepsilon^{j+1}_{i,\lambda}$and T_i^{j+1}. This system is indeterminate because it has only a single equation for each pixel per band. Thus, it cannot be solved directly. To address this, we increase the number of equations by assuming that any component i in adjacent pixels has the same $\varepsilon^{j+1}_{i,\lambda}$ and T_i^{j+1} for each band λ. Therefore, by considering a window of M pixels, the total number of equations in the system becomes $M \times N_{\text{spectral bands}}$. The full equation system can be written as Eq.(3).

2.2.3 Spectral Correlation (SC) Module: It identifies and rectifies erroneous pixels (*i.e.*, T_i^{j+1} and $\varepsilon^{j+1}_{i,\lambda}$) for each component i. This is very useful if the retrieved optical / temperature properties of some components are outside the range of standard values. Optical / temperature rules for each component can be customized, enabling the detection and removal of these erroneous pixels. This is done with operators whose priority is set by parentheses:

- Arithmetic operators: addition (+), subtraction (−), multiplication (*), and division (/).
- Relational operators: greater than (>), greater than or equal to (>=), less than (<), and less than or equal to (<=).
- Logical operators: and (&), or (|).

In the context of emissivity, comparisons can be made between different bands for the same component and between components. For instance, one can specify that vegetation emissivity at 9 µm must be lower than that at 8 µm. One can also specify that water must have a lower or higher temperature than the ground, depending on whether it is a daytime or nighttime satellite image. Pixels inconsistent with spectral correlation rules are set to NaN values and subsequently eliminated using the median filter. This ensures the accuracy and reliability of the data.

$$\begin{pmatrix} L_{\mathrm{sat},\lambda}(1) \\ \dots \\ L_{\mathrm{sat},\lambda}(M) \end{pmatrix} = \begin{pmatrix} L^j_{\mathrm{DART},\lambda}(1) \\ \dots \\ L^j_{\mathrm{DART},\lambda}(M) \end{pmatrix} - \begin{pmatrix} \sum_{i=1}^{I}\left[G^j_{\varepsilon,i,\lambda}(1).\varepsilon^j_{i,\lambda}(1) + G^j_{T,i,\lambda}(1).T^j_i(1)\right] \\ \dots \\ \sum_{i=1}^{I}\left[G^j_{\varepsilon,i,\lambda}(M).\varepsilon^j_{i,\lambda}(M) + G^j_{T,i,\lambda}(M).T^j_i(M)\right] \end{pmatrix} +$$

$$\begin{pmatrix} G^j_{T,1,\lambda}(1) & .. & G^j_{T,I,\lambda}(1) & G^j_{\varepsilon,1,\lambda}(1) & .. & G^j_{\varepsilon,I,\lambda}(1) & G^j_{\varepsilon,I,\lambda}(1) & .. & G^j_{\varepsilon,I,\lambda}(1) \\ G^j_{T,1,\lambda}(2) & .. & G^j_{T,I,\lambda}(2) & G^j_{\varepsilon,1,\lambda}(2) & .. & G^j_{\varepsilon,I,\lambda}(2) & G^j_{\varepsilon,I,\lambda}(2) & .. & G^j_{\varepsilon,I,\lambda}(2) \\ \vdots & \ddots & \ddots & \ddots & \ddots & \ddots & \ddots & \ddots & \vdots \\ G^j_{T,1,\lambda}(M) & .. & G^j_{T,I,\lambda}(M) & G^j_{\varepsilon,1,\lambda}(M) & .. & G^j_{\varepsilon,I,\lambda}(M) & G^j_{\varepsilon,I,\lambda}(M) & .. & G^j_{\varepsilon,I,\lambda}(M) \end{pmatrix} \cdot \begin{pmatrix} T_1^{j+1} \\ \dots \\ T_I^{j+1} \\ \varepsilon^{j+1}_{1,\lambda} \\ \dots \\ \varepsilon^{j+1}_{I,\lambda} \\ \varepsilon^{j+1}_{I,\lambda} \\ \dots \\ \varepsilon^{j+1}_{I,\lambda} \end{pmatrix}, \quad (3)$$

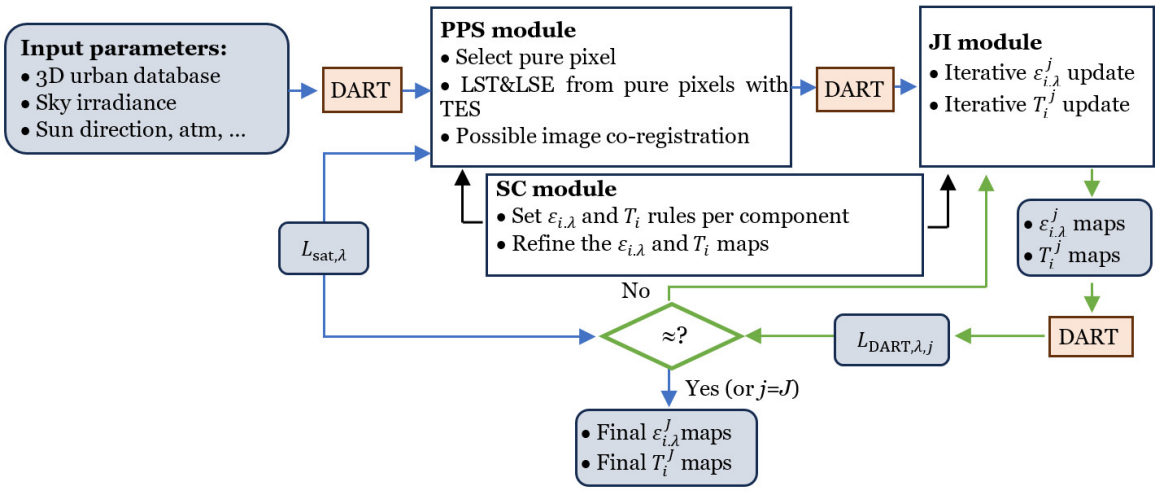

Figure 1. Algorithm flow chart: input and output parameters (rounded rectangle), processes (square corner rectangle), decision (diamond), DART inversion (blue), simulation (red) and loop flow (green). j: current iteration. J: maximum iteration. $L_{\mathrm{sat},\lambda}$: satellite at-surface radiance image at band λ. $L_{\mathrm{DART},\lambda,j}$: DART radiance image at band λ at iteration j. $\varepsilon_{i,\lambda,j}$: emissivity of component i at band λ at iteration j. $T_{i,j}$: temperature of component i at iteration j. PPS: pure pixel selection; JI: Jacobian iteration; SC: spectral correlation.

2.3 Data

2.3.1 The 3D Mock-up: TRUST-DART accuracy and reliability are assessed using two scenes. (1) A DART-created schematic 3D vegetation mock-up with vegetation and ground components. (2) A realistic 3D urban mock-up representing a European city, Brussels in Belgium.

The vegetation scene is a 30 m × 20 m zone simulated at 1 m spatial resolution, with three homogeneous 10 m × 10 m maize fields at three growth stages with two Leaf Angle Distributions (LADs) - Spherical and Plagiophile (Figure 2). As the growth stage increases, the Leaf Area Index (LAI) increases from 0.95 to 5.00, and maize height increases from 0.55 m to 1.95 m. Maize parameters are taken from the literature (Duthoit et al., 2008).

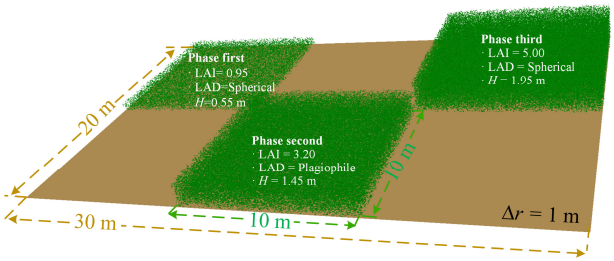

Figure 2. The vegetation scene: bare ground and 3 maize fields at 3 growth stages with their height (H), leaf area index (LAI), and leaf angle distribution (LAD). DART spatial resolution is 1 m.

The urban scene, Brussels, is the focus of this study (Figure 3). It is at 50° 51′ 0″ N, 4° 21′ 0″ E in the north-central part of Belgium, at 54 m mean altitude, from 10 m to 121 m. Its 3D mock-up is from Urbis (https://datastore.brussels/web/urbis-download). After its conversion to OBJ format, it is merged into a single file, and errors such as misclassified roofs and holes in the DEM (Digital Elevation Model) are corrected using specifically designed algorithms and Blender software. Finally, the 3D mock-up is converted from the national geo-reference system (EPSG:31370) to the international system (EPSG:32361).

Brussels is a densely populated urban area with a mean Urban Heat Island (UHI) effect of 3.22 °C, especially at night, with heat waves likely to become more frequent (Lauwaet et al., 2016). Deriving the emissivity and temperature of urban components from satellite images is essential to simulate the urban radiative budget, for instance, with a 3D model such as DART.

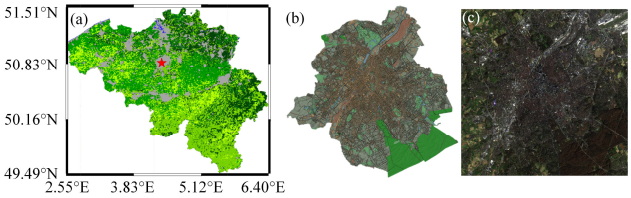

Figure 3. The urban site. a) MODIS yearly land-cover map of Belgium with Brussels (★). b) Brussels 3D mock-up (water: blue; vegetation: green; ground: yellow; building: black); c) RGB true color composite of Brussels (PlanetScope image).

2.3.2 Optical and Temperature Properties: TRUST-DART accuracy is accessed through its application on pseudo-ASTER images that DART simulates using optical and temperature properties of landscape components (Table 1) from the literature (Zhen et al., 2022). The authors selected representative optical properties from the ASTER or DART spectral database in this referenced work. These properties are then resampled using the ASTER spectral response function to simulate ASTER images for TES accuracy assessment.

In TRUST-DART, each component in a pixel is assumed to have constant optical and temperature properties. This is a challenge when validating accuracy for components with two temperatures, as in neighbor illuminated and shaded areas. To address this, we introduce simplifications when simulating the pseudo-ASTER image: the optical and temperature properties of each component are isotropic and spatially invariant. Each component is assigned a single emissivity library and a constant temperature value across the entire scene. As a result, pseudo-ASTER images do not have spectral confusion issues.

Components	T_i (K)	$\varepsilon_{\lambda,i}$				
		8.3µm	8.65µm	9.1µm	10.6µm	11.3µm
Vegetation	305.65	0.9726	0.9656	0.9573	0.9597	0.9628
Ground	311.65	0.9828	0.9822	0.9781	0.9703	0.9669

Table 1. Emissivity ($\varepsilon_{\lambda,i}$) and temperature (T_i) to simulate ASTER pseudo image. $\varepsilon_{\lambda,i}$ is resampled to ASTER spectral sensitivity.

2.3.3 Satellite Data and Preprocessing: TRUST-DART is tested with ASTER satellite images of Brussels. Table 2 shows its date, spectral bands, and spatial resolution.

Parameters	Values		
ID	00309262018212643		
Time	2018.09.26 21:26:43		
Bands	λ (µm)	$\Delta\lambda$ (µm)	Δr (m)
B1	8.300	0.350	90
B2	8.650	0.350	90
B3	9.100	0.350	90
B4	10.600	0.700	90
B5	11.300	0.700	90

Table 2. ASTER image information of Brussels: date and bands (central wavelength λ, spectral bandwidth $\Delta\lambda$). Spatial resolution Δr = 90 m. Data from USGS (https://lpdaac.usgs.gov/data/get-started-data/collection-overview/missions/aster-overview/).

The preprocessing of images involves two key steps: reprojection and co-registration. To minimize the impact of resampling on the spectral data of the image, we project the urban 3D mock-up to its satellite image coordinates, WGS 1984 UTM Zone 31N. For co-registrating the ASTER and DART images, we use the GeFolki software (Brigot et al., 2016; Plyer et al., 2015), a product of the French Space Agency (https://w3.onera.fr/medusa/gefolki). This software claims a geometric accuracy of 0.1 pixels. However, it is essential to note that any unavoidable inaccuracies in co-registration could potentially deteriorate the precision of inversion.

3. Application and Accuracy Assessment

3.1 Application on Simulated Vegetation Plots Scene

3.1.1 Visual Accuracy Assessment: We use false RGB color composites to display the differences between pseudo-ASTER images and images simulated by DART using the maps of temperature and emissivity per scene component. Figure 4 shows the pseudo-ASTER image (Figure 4.a) and DART simulated image after inversion (Figure 4.b). These images are visually

very similar, particularly the pure ground pixels. We can note a slight difference for vegetation: The vegetation in the DART simulated image after inversion appears slightly lighter than the pseudo-ASTER image.

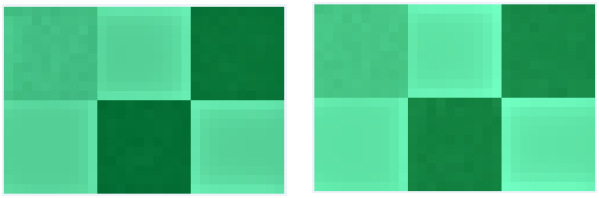

(a) Pseudo ASTER image (b) DART image after inversion

Figure 4. Vegetation plots images using false RGB composition. (a) Pseudo ASTER image. (b) DART simulated image using emissivity and temperature from TRUST-DART.

3.1.2 Quantitative Accuracy Assessment: TRUST-DART emissivity and radiance relative error and temperature residual error are quantified by two statistical parameters: median error ± interquartile range (Figure 5) and mean error ± standard deviation (Figure 6). They depict how the error distribution evolves with iterations. Nearly every median error showed a decreasing trend with iterations (Figure 5). For the mean error (Figure 6), although radiance and temperature errors show a stable decreasing trend, emissivity error fluctuates. This is because certain components in pixels (such as soil covered by vegetation) contribute less to the pixel radiance, making retrieving temperature and emissivity more difficult. However, even if these errors are relatively large, their impacts on the radiance error of the pixel are minimal.

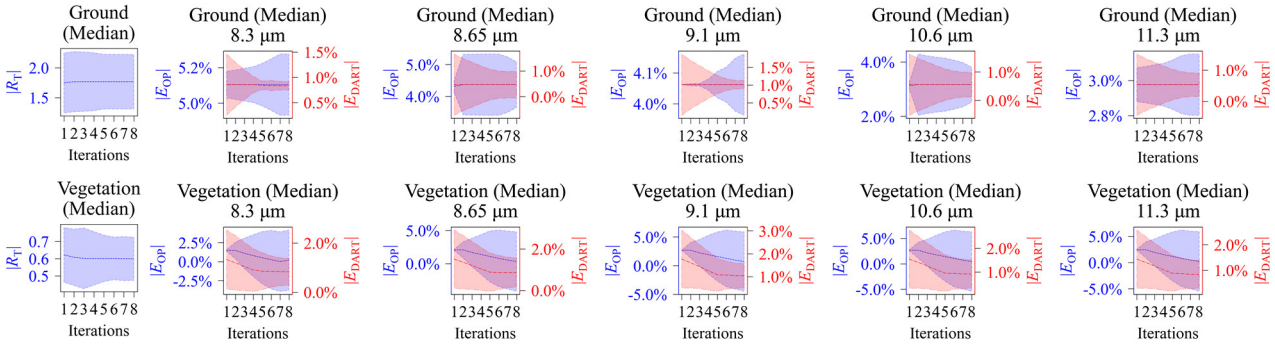

Figure 5. Accuracy assessment of component temperature, emissivity, and pixel radiance by the absolute value of the median error indicator. Temperature error (R_T) is assessed using the residual error. Radiance (E_{DART}) and emissivity (E_{OP}) errors are assessed using the relative error. The values used to simulate the pseudo-ASTER image are considered true values, and the values retrieved by TRUST-DART are considered estimated values.

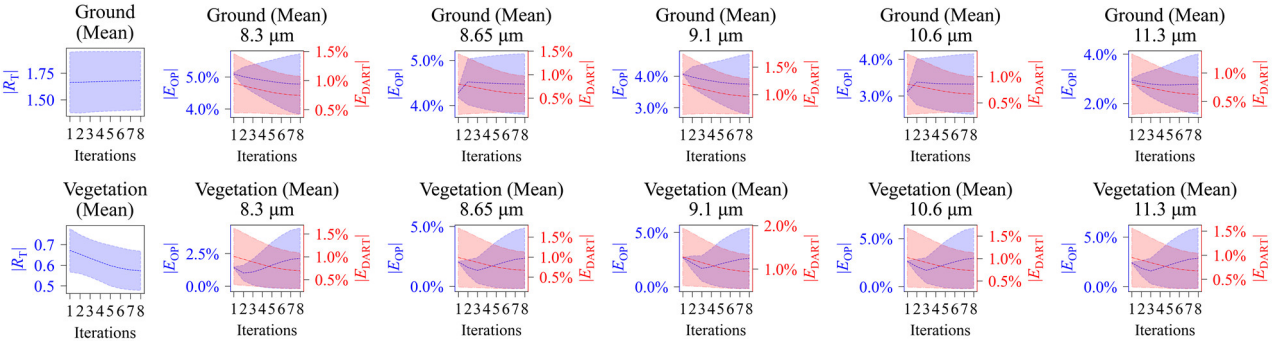

Figure 6. Accuracy assessment of component temperature, emissivity, and pixel radiance by the absolute value of the mean error indicator. Temperature error (R_T) is assessed using the residual error. Radiance (E_{DART}) and emissivity (E_{OP}) errors are assessed using the relative error. The values used to simulate the pseudo-ASTER image are considered true values, and the values retrieved by TRUST-DART are considered estimated values.

3.2 Application on Realistic Urban Scene

3.2.1 Visual Accuracy Assessment: The ASTER images are used to assess the accuracy of the TRUST-DART. Here, RGB false color composites are used to visually compare the ASTER and DART images simulated with temperature and emissivity maps derived from TRUST-DART. The ASTER image (Figure 7.a) and the DART simulated image after inversion (Figure 7.b) are very similar. The DART simulated image is sharper than the ASTER image, probably due to the modulation transfer function and atmospheric effects.

3.2.2 Quantitative Accuracy Assessment: Figure 8 and Figure 9 show that no matter the median or mean error, the error of pixel radiance always decreases with the iterations for all bands. In addition, the median error shows a much clearer decrease trend than the mean error, similar to the vegetation case. In contrast, the final convergence accuracy is different for distinct bands. Depending on the mean radiance, usually low radiance (shorter wavelength) bands produce a high relative error.

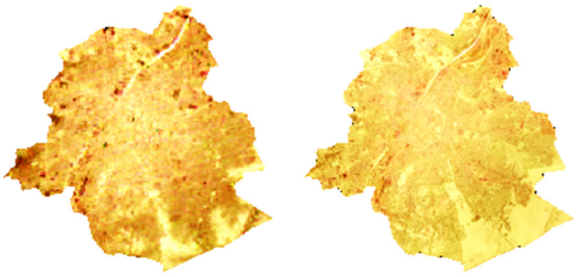

(a) ASTER image (b) DART image after inversion

Figure 7. Brussels false RGB composite images. a) ASTER image. b) DART image simulated with emissivity and temperature from TRUST-DART.

4. Discussion and Conclusions

4.1 Discussion

4.1.1 Advantages: This study introduces TRUST-DART, a versatile, physical-based, nonlinear thermal unmixing model that eliminates many restrictions faced by existing TIR unmixing methods. Unlike traditional methods, TRUST-DART does not require strict spatial, spectral, and temporal resolutions, angular or land cover requirements, a priori field measurements, or manual operations. It offers better physical interpretability than neural network models by transferring gradients between parameters with clear physical meanings. TRUST-DART requires fewer satellite requirements and can separate component emissivity and temperature simultaneously, providing spatially varying maps. TRUST-DART is compatible with other TES-based methods and can enhance its accuracy by incorporating advanced TES methods (Michel et al., 2021), making it sensor-independent and versatile for various sensors. It also introduces a 3D mock-up for nonlinear thermal infrared unmixing, which can be suitable for heterogeneous areas.

4.1.2 Limitations: TRUST-DART faces limitations due to its reliance on spatial correlation-based multi-pixel unmixing methods, which require adjacent pixels with varying surface parameters. In homogeneous scenes, like vegetation plots, strong linear correlations complicate equation-solving, and autocorrelations among neighboring pixels reduce spatial resolution when decomposing component temperatures (Zhan et al., 2013). It also cannot detect variations in temperature and emissivity within a single pixel. The use of a 3D mock-up can lead to geometry misregistration and viewing angle variations, impacting the accuracy of separated component properties. Although TRUST-DART requires a 3D mock-up, with urban mock-ups becoming more and more commonly available (https://blender-addons.org/blosm/) and the booming plant 3D architecture modeling (Zhen et al., 2024), 3D radiative transfer modeling has also gained wider application. We use ASTER images at 90 m spatial resolution, with almost no completely pure pixels in Brussels. This potentially compromises the accuracy of the PPS module. Higher spatial resolution imagery may help to ameliorate this problem.

4.2 Conclusions

We propose the TRUST-DART model for separating component emissivity and temperature from surface TIR multispectral images. TRUST-DART is free from the common problems of the TIR unmixing methods, such as spatial, spectral, temporal resolution, angular, scene, field measurement requirements, or even manual operations. TRUST-DART has three modules: PPS, JI, and SC. Its validation is carried out using a DART-created schematic vegetation cover and the realistic urban 3D mock-up of Brussels, Belgium. TRUST-DART may suffer from some common problems faced by multi-pixel and multi-source data. TRUST-DART is robust for high-fraction components, but its accuracy decreases with lower fractions.

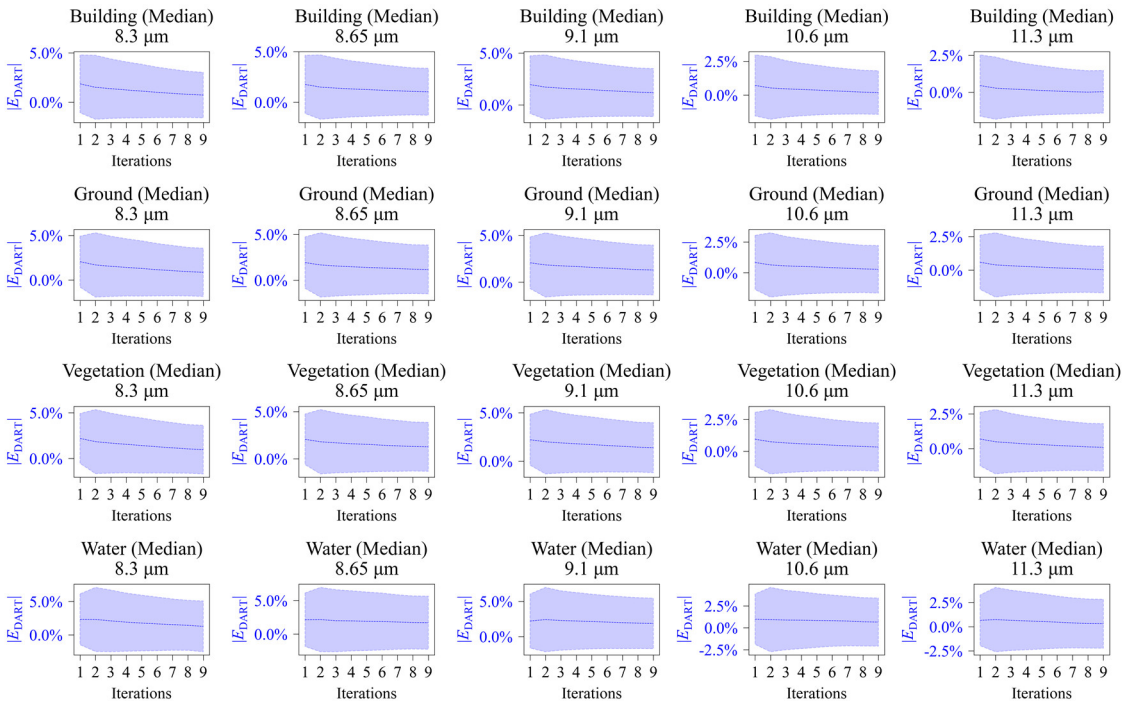

Figure 8. Accuracy assessment of DART simulated pixel radiance by the median relative error (E_{DART}) absolute value relative to ASTER pixels.

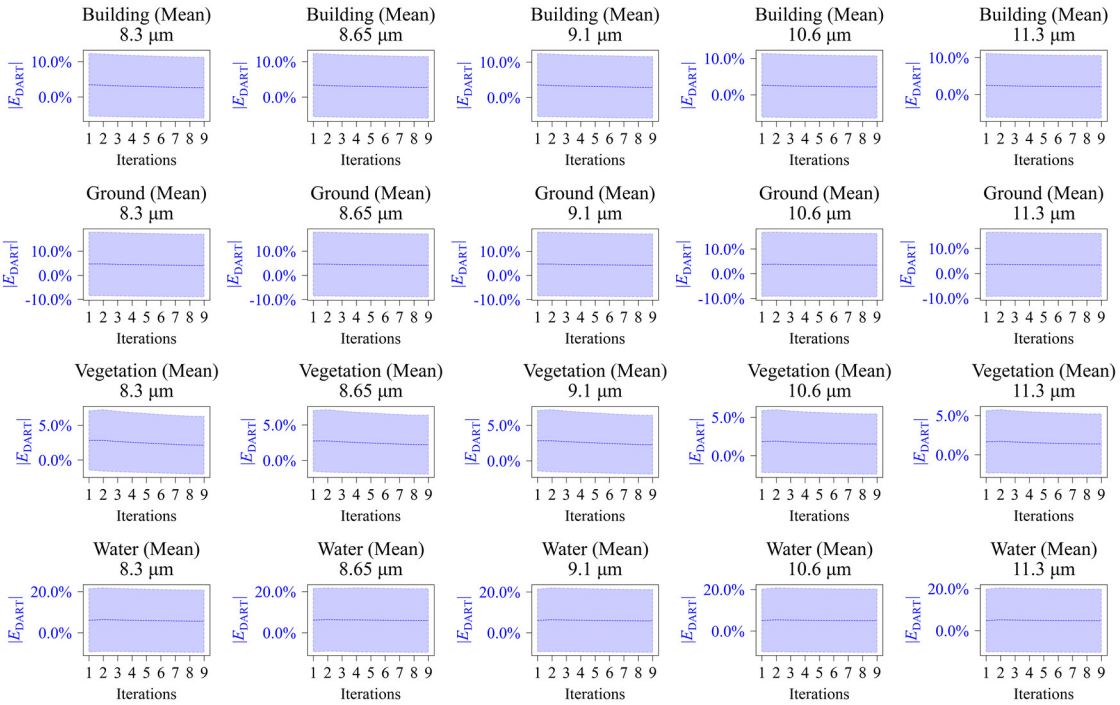

Figure 9. Accuracy assessment of DART simulated pixel radiance by the mean relative error (E_{DART}) absolute value relative to ASTER pixels.

Acknowledgements

The authors thank the National Natural Science Foundation of China (NSFC, grant 42201372), the Belgium Science Policy Office BELSPO STEREO IV Programme (contract SR/67/408), and the TOSCA program of the French Space Center (CNES). The authors thank Robbe Neyns from Vrije Universiteit Brussel for providing Brussels's tree geometry and location data. The authors thank Lucas Landier from CNES for his innovative ideas on the inversion of satellite images.

References

Archer, N., Jones, H., 2006. Integrating hyperspectral imagery at different scales to estimate component surface temperatures. *Int. J. Remote Sens.*, 27, 2141-2159.

Brigot, G., Colin-Koeniguer, E., Plyer, A., Janez, F., 2016. Adaptation and evaluation of an optical flow method applied to coregistration of forest remote sensing images. *IEEE J. Sel. Top. Appl. Earth Observ.*, 9, 2923-2939.

Cao, B., Liu, Q., Du, Y., Roujean, J.-L., Gastellu-Etchegorry, J.-P., Trigo, I.F., Zhan, W., Yu, Y., Cheng, J., Jacob, F., 2019. A review of earth surface thermal radiation directionality observing and modeling: Historical development, current status and perspectives. *Remote Sens. Environ.*, 232, 111304.

Chen, J.M., Liu, J., 2020. Evolution of evapotranspiration models using thermal and shortwave remote sensing data. *Remote Sens. Environ.*, 237, 111594.

Chrysoulakis, N., Grimmond, S., Feigenwinter, C., Lindberg, F., Gastellu-Etchegorry, J.-P., Marconcini, M., Mitraka, Z., Stagakis, S., Crawford, B., Olofson, F., 2018. *Urban energy exchanges monitoring from space. Sci. Rep.*, 8, 1-8.

Cubero-Castan, M., Chanussot, J., Achard, V., Briottet, X., Shimoni, M., 2014. A physics-based unmixing method to estimate subpixel temperatures on mixed pixels. *IEEE Trans. Geosci. Remote Sens*, 53, 1894-1906.

Dozier, J., 1981. A method for satellite identification of surface temperature fields of subpixel resolution. *Remote Sens. Environ.*, 11, 221-229.

Duthoit, S., Demarez, V., Gastellu-Etchegorry, J.-P., Martin, E., Roujean, J.-L., 2008. Assessing the effects of the clumping phenomenon on BRDF of a maize crop based on 3D numerical scenes using DART model. *Agric. For. Meteorol.*, 148, 1341-1352.

Fontanilles, G., Briottet, X., 2011. A nonlinear unmixing method in the infrared domain. *Appl. Opt.*, 50, 3666-3677.

Gastellu-Etchegorry, J., Lauret, N., Tavares, L., Lamquin, N., Bruniquel, V., Roujean, J., Hagolle, O., Zhen, Z., Wang, Y., Regaieg, O., 2022. Correction of Directional Effects in Sentinel-2 and-3 Images with Sentinel-3 Time Series and Dart 3D Radiative Transfer Model, *IEEE International Geoscience and Remote Sensing Symposium. IEEE,* pp. 4563-4566.

Gastellu-Etchegorry, J., Wang, Y., Regaieg, O., Yin, T., Malenovsky, Z., Zhen, Z., Yang, X., Tao, Z., Landier, L., Al Bitar, A., 2020a. Recent Improvements in the Dart Model for Atmosphere, Topography, Large Landscape, Chlorophyll Fluorescence, Satellite Image Inversion, *IEEE International Geoscience and Remote Sensing Symposium. IEEE*, pp. 3455-3458.

Gastellu-Etchegorry, J., Wang, Y., Regaieg, O., Yin, T., Malenovsky, Z., Zhen, Z., Yang, X., Tao, Z., Landier, L., Al Bitar, A., 2020b. Why To Model Remote Sensing Measurements In 3d? Recent Advances In Dart: Atmosphere, Topography,

Large Landscape, Chlorophyll Fluorescence And Satellite Image Inversion, in *Proc. Int. Conf. Adv. Technol. Signal Image Process. (ATSIP). IEEE*, pp. 1-6.

Gillespie, A., Rokugawa, S., Matsunaga, T., Cothern, J.S., Hook, S., Kahle, A.B., 1998. A temperature and emissivity separation algorithm for Advanced Spaceborne Thermal Emission and Reflection Radiometer (ASTER) images. *IEEE Trans. Geosci. Remote Sens*, 36, 1113-1126.

Gillespie, A.R., 1992. Spectral mixture analysis of multispectral thermal infrared images. *Remote Sens. Environ.*, 42, 137-145.

Granero-Belinchon, C., Michel, A., Achard, V., Briottet, X., 2020. Spectral unmixing for thermal infrared multi-spectral airborne imagery over urban environments: day and night synergy. *Remote Sens.*, 12, 1871.

Hu, T., Mallick, K., Hulley, G.C., Planells, L.P., Göttsche, F.M., Schlerf, M., Hitzelberger, P., Didry, Y., Szantoi, Z., Alonso, I., 2022. Continental-scale evaluation of three ECOSTRESS land surface temperature products over Europe and Africa: Temperature-based validation and cross-satellite comparison. *Remote Sens. Environ.*, 282, 113296.

Huang, F., Zhan, W., Wang, Z., Wang, K., Chen, J.M., Liu, Y., Lai, J., Ju, W., 2017. Positive or negative? Urbanization‐induced variations in diurnal skin‐surface temperature range detected using satellite data. *J. Geophys. Res.: Atmos.*, 122, 13,229-213,244.

Jacob, F., Schmugge, T., Olioso, A., French, A., Courault, D., Ogawa, K., Petitcolin, F., Chehbouni, G., Pinheiro, A., Privette, J., 2008. Modeling and inversion in thermal infrared remote sensing over vegetated land surfaces. *Advances in land remote sensing: System, modeling, inversion and application*, 245-291.

Jiang, Y., Tang, R., Li, Z.-L., 2022. A framework of correcting the angular effect of land surface temperature on evapotranspiration estimation in single-source energy balance models. *Remote Sens. Environ.*, 283, 113306.

Kimes, D., 1983. Remote sensing of row crop structure and component temperatures using directional radiometric temperatures and inversion techniques. *Remote Sens. Environ.*, 13, 33-55.

Landier, L., Gastellu-Etchegorry, J., Al Bitar, A., Chavanon, E., Lauret, N., Feigenwinter, C., Mitraka, Z., Chrysoulakis, N., 2018. Calibration of urban canopies albedo and 3D shortwave radiative budget using remote-sensing data and the DART model. *Eur. J. Remote Sens.*, 51, 739-753.

Lauwaet, D., De Ridder, K., Saeed, S., Brisson, E., Chatterjee, F., Van Lipzig, N., Maiheu, B., Hooyberghs, H., 2016. Assessing the current and future urban heat island of Brussels. *Urban Climate*, 15, 1-15.

Li, X., Strahler, A.H., Friedl, M.A., 1999. A conceptual model for effective directional emissivity from nonisothermal surfaces. *IEEE Trans. Geosci. Remote Sens*, 37, 2508-2517.

McMillin, L.M., 1975. Estimation of sea surface temperatures from two infrared window measurements with different absorption. *J. Geophys. Res.*, 80, 5113-5117.

Michel, A., Granero-Belinchon, C., Cassante, C., Boitard, P., Briottet, X., Adeline, K.R., Poutier, L., Sobrino, J.A., 2021. A New Material-Oriented TES for Land Surface Temperature and SUHI Retrieval in Urban Areas: Case Study over Madrid in the Framework of the Future TRISHNA Mission. *Remote Sens.*, 13, 5139.

Norman, J.M., Becker, F., 1995. Terminology in thermal infrared remote sensing of natural surfaces. *Agric. For. Meteorol.*, 77, 153-166.

Ottlé, C., Vidal-Madjar, D., 1992. Estimation of land surface temperature with NOAA9 data. *Remote Sens. Environ.*, 40, 27-41.

Plyer, A., Colin-Koeniguer, E., Weissgerber, F., 2015. A new coregistration algorithm for recent applications on urban SAR images. *IEEE Geosci. Remote S*, 12, 2198-2202.

Ru, C., Duan, S.-B., Jiang, X.-G., Li, Z.-L., Huang, C., Liu, M., 2023. An extended SW-TES algorithm for land surface temperature and emissivity retrieval from ECOSTRESS thermal infrared data over urban areas. *Remote Sens. Environ.*, 290, 113544.

Sánchez, J., Kustas, W., Caselles, V., Anderson, M., 2008. Modelling surface energy fluxes over maize using a two-source patch model and radiometric soil and canopy temperature observations. *Remote Sens. Environ.*, 112, 1130-1143.

Sobrino, J., Romaguera, M., 2004. Land surface temperature retrieval from MSG1-SEVIRI data. *Remote Sens. Environ.*, 92, 247-254.

Song, L., Bian, Z., Kustas, W.P., Liu, S., Xiao, Q., Nieto, H., Xu, Z., Yang, Y., Xu, T., Han, X., 2020. Estimation of surface heat fluxes using multi-angular observations of radiative surface temperature. *Remote Sens. Environ.*, 239, 111674.

Wan, Z., Li, Z., 1997. A physics-based algorithm for retrieving land-surface emissivity and temperature from EOS/MODIS data. *IEEE Trans. Geosci. Remote Sens*, 35, 980-996.

Wang, Y., Kallel, A., Zhen, Z., Lauret, N., Guilleux, J., Chavanon, E., Gastellu-Etchegorry, J.-P., 2024. 3D Monte Carlo differentiable radiative transfer with DART. *Remote Sens. Environ.*, 308, 114201.

Watson, K., 1992. Two-temperature method for measuring emissivity. *Remote Sens. Environ.*, 42, 117-121.

Zhan, W., Chen, Y., Voogt, J.A., Zhou, J., Wang, J., Ma, W., Liu, W., 2012. Assessment of thermal anisotropy on remote estimation of urban thermal inertia. *Remote Sens. Environ.*, 123, 12-24.

Zhan, W., Chen, Y., Zhou, J., Wang, J., Liu, W., Voogt, J., Zhu, X., Quan, J., Li, J., 2013. Disaggregation of remotely sensed land surface temperature: Literature survey, taxonomy, issues, and caveats. *Remote Sens. Environ.*, 131, 119-139.

Zhen, Z., Benromdhane, N., Kallel, A., Wang, Y., Regaieg, O., Boitard, P., Landier, L., Chavanon, E., Lauret, N., Guilleux, J., 2023. DART: a 3D radiative transfer model for urban studies,

2023 *Joint Urban Remote Sensing Event (JURSE). IEEE*, pp. 1-4.

Zhen, Z., Chen, S., Yin, T., Gastellu-Etchegorry, J.-P., 2022. Spatial Resolution Requirements for the Application of Temperature and Emissivity Separation (TES) Algorithm over Urban Areas. *IEEE J. Sel. Top. Appl. Earth Observ.*, 15, 8990-9003.

Zhen, Z., Chen, S., Yin, T., Han, C., Chavanon, E., Lauret, N., Guilleux, J., Gastellu-Etchegorry, J.-P., 2024. A Dynamic L-system based Architectural Maize Model for 3D Radiative Transfer Simulation. *IEEE Trans. Geosci. Remote Sens*, 62, 4401620.

Zhen, Z., Gastellu-Etchegorry, J.-P., Chen, S., Yin, T., Chavanon, E., Lauret, N., Guilleux, J., 2021. Quantitative Analysis of DART Calibration Accuracy for Retrieving Spectral Signatures Over Urban Area. *IEEE J. Sel. Top. Appl. Earth Observ.*, 14, 10057-10068.